ENGINEERING

Twirlbot: Tumbleweed-inspired rolling robot

Chi Chen[1], Zhuo Wang[1], Yuchen Wang[2], Pengju Shi[1], Zixiao Liu[1], Muqing Si[1], Sidi Duan[1], Wenhao Hou[1], Ximin He[1]*

Omnidirectional locomotion offers superior adaptability and maneuverability over uni-/bidirectional movement, with spherical structures being ideal due to their zero turning radius and geometric stability on complex terrains. However, existing spherical robots rely on embedded control components and onboard power sources, inevitably increasing design complexity, weight, and cost. Herein, we developed a tumbleweed-inspired rolling robot (Twirlbot) to achieve the hollow spherical architecture by weaving photoactive/passive bilayer strips. The Twirlbot demonstrated autonomous rolling under constant light, enabling multiple functionalities, including omnidirectional locomotion, slope climbing, trampling resistance, cargo transport, self-correction, wind resistance, and adaptation to diverse terrains and environments. These features endowed the Twirlbot with great potential for real-world applications, such as self-sustained seed-sowing, daylight-driven commuting, and autonomous underwater wiring. Notably, the structural design was generalizable to other systems, including commercial materials, enabling substantial cost reduction (less than one-tenth that of existing autonomous untethered robots) and thereby presenting a promising route toward next-generation untethered, self-sustained robotic systems.

INTRODUCTION

Unidirectional movement is the most fundamental locomotion in nature and robotics. Rolling, an efficient motion mode with low friction, is widely used in toroidal/cylinder-shaped designs (*1*). However, effective navigation across complex real-world terrains requires steering capability and thus necessitates multidirectional rotary motility, which is typically achieved through elaborate control systems (e.g., differential drive) (*2*) or specialized structures (e.g., Mecanum wheels) (*3*). As an ultimate goal, omnidirectional rolling with a minimal turning radius becomes particularly powerful, offering high flexibility and maneuverability when the vehicle encounters obstacles, especially in narrow spaces. Compared with wheel-shaped structures, spherical rollers, especially those constructed from soft materials, are intrinsically free from turning radius, enable infinite rolling directions, and exhibit geometric stability that prevents them from tipping over or getting stuck on obstacles (*4*). Moreover, with the entire system enclosed within its shell, the spherical architecture not only protects its inner components but also leverages material compliance and structural deformation to enlarge the contact area and reduce the ground pressure, while its continuous curvature lowers shear forces and enhances lift in granular media (e.g., sand, snow, and vegetation) (*5*). These effects minimize the damage to soft substrate surfaces and enable locomotion on delicate terrains (*6*). Nevertheless, the existing spherical robots are almost exclusively driven by internal multicomponent systems, including motor, processor, and tethered power (*7*). This results in high design complexity for maintaining dynamic balance and increased difficulty in replacing malfunctioning components. Consequently, the miniaturization, cost efficiency, and long-term operational robustness of such omnidirectional robots can be extremely challenging.

Stimuli-responsive polymers—including liquid crystal polymers (LCPs), liquid crystal elastomers (LCEs), and materials with high coefficients of thermal expansion—represent a class of physically intelligent materials capable of large, reversible deformations, offering a promising solution at the material level (*8*, *9*). Such intelligence enables seamless integration of sensing, decision-making, and actuation within a monolithic material and eliminates the need for a tethered power, which substantially reduces the system complexity and enhances robustness (*10*–*12*). For instance, carefully designed LCP actuators can harness the untethered light to perform self-continuous locomotions, including unidirectional rolling (*13*), undulatory motion (*14*), and oscillation-driven movement (*15*). However, these designs are limited to one or a few locomotive directions due to limited alignment orientation within their twisted ribbon, cylinder, or wheel-like structure (*16*–*18*). In the meantime, a light-powered tensegrity robot, composed of rigid rods as the exoskeleton and LCEs as actuators, has achieved multidirectional locomotion based on its polyhedral geometry, which enables a greater diversity of alignment orientations and corresponding deformation directions. Nevertheless, manual control of light incidence is required to guide its direction, as each step necessitates readjusting the incidence angle of illumination to selectively activate different LCE fiber-like actuators (*19*). To date, autonomous omnidirectional rolling has remained elusive in existing soft robotic designs, as the limited alignment orientations of highly deformable stimuli-responsive materials persist, and a symmetrically spherical configuration has yet to be achieved in such systems.

Tumbleweed, an organism that relies on rolling as the primary moving mode, inspires us in both kinematics and geometric fabrication. Before reaching maturity, the tumbleweed grows in a rounded skeleton of a shrub, while a specialized layer of cells allows the plant to detach from its roots when the humidity falls below the survivable level. Owing to the hollow spherical geometry, it can harness the wind force from the surrounding environment to disperse up to 250,000 seeds across wide areas (*6*), with dispersal distances exceeding 1 kilometer (Fig. 1A) (*20*). To fabricate such a symmetric spherical structure, we hypothesize that the weaving method using photoactive strips can be used (*21*). In this approach, each strip is independent yet physically interlaced to support the others, resembling the hollow architecture of tumbleweeds formed by interlocked branches. As a result, actuation of the irradiated region would also trigger motion in neighboring strips through mechanical interlocking, which leads to the total moment change for falling over and thereby

[1]Department of Materials Science and Engineering, University of California, Los Angeles, Los Angeles, CA 90095, USA. [2]Department of Mechanical and Aerospace Engineering, University of California, Los Angeles, Los Angeles, CA 90095, USA.
*Corresponding author. Email: ximinhe@ucla.edu

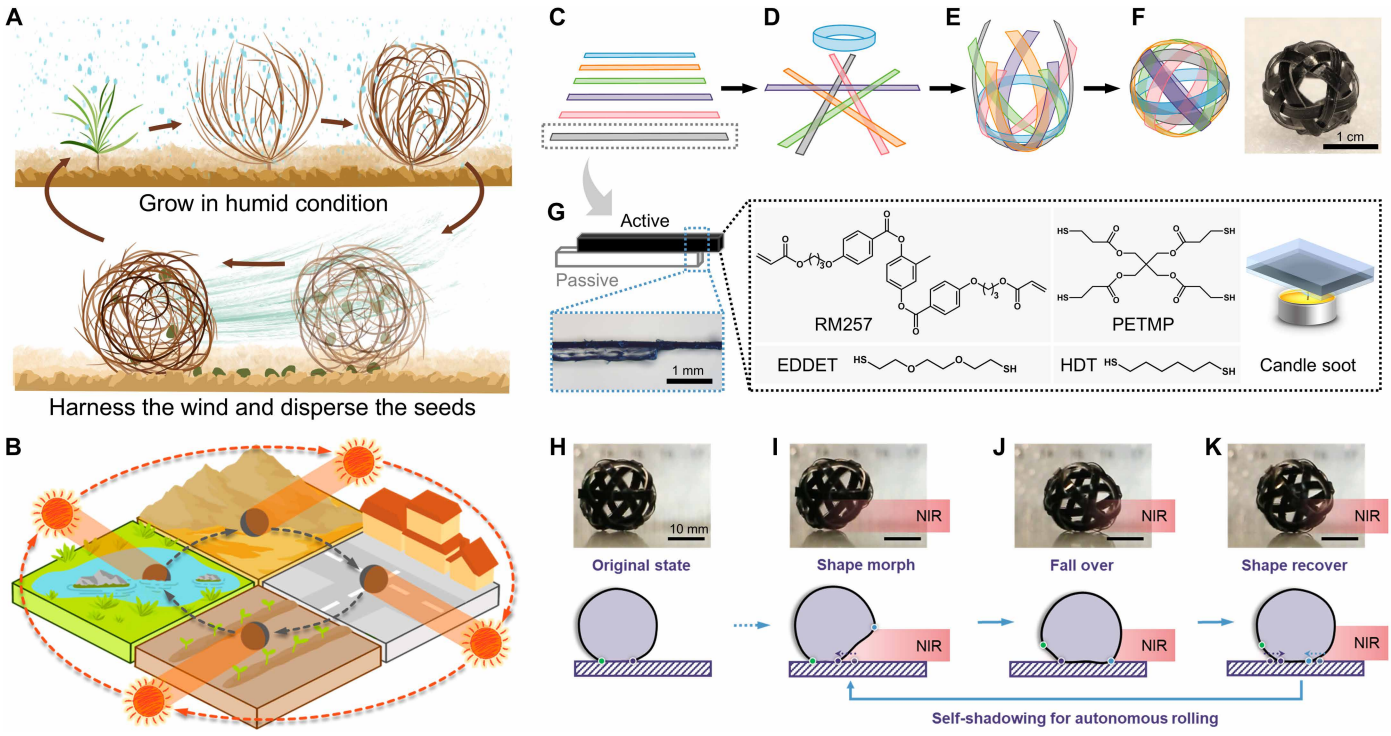

Fig. 1. Fabrication and rolling mechanism of the Twirlbot. (**A**) The life cycle of a natural tumbleweed and its rolling movement by harnessing the wind. (**B**) The Twirlbot capable of autonomous omnidirectional rolling fueled by constant light across various terrains. (**C** to **F**) The fabrication process of Twirlbot into an interwoven hollow sphere, based on (**G**) six identical active/passive bilayer strips. (**H** to **K**) Self-sustained rolling process and mechanism under constant near-infrared (NIR) irradiation.

generates rolling motion. Because the rolling motion exposes new regions to the constant light, autonomous continuous locomotion could be achieved. Moreover, such woven structures with mechanical entanglement of weft and warp strips have demonstrated outstanding payload-to-weight ratios. For instance, a polyethylene terephthalate-based soft gripper has achieved a ratio of ~770 times (*22*), highlighting their high load-carrying capacity and lightweight properties of these designs (*23*).

Herein, we proposed a general strategy for developing a tumbleweed-inspired rolling robot (Twirlbot) through the weaving method of fabricating six identical photoactive/passive bilayer strips [e.g., LCE/polydimethylsiloxane (PDMS)]. Free from additional control and power components, the resulting symmetrically spherical Twirlbot was capable of light-fueled self-sustained omnidirectional locomotion and exhibited distinct elastic deformability and robustness, which were highly advantageous for practical applications (Fig. 1B). Specifically, it achieved climbing, trampling resistance, cargo transportation, self-correction, wind resistance, and autonomous rolling across multiple terrains, with its capabilities even extending to aquatic environments. Moreover, the Twirlbot reproduced the seed-dispersal behavior of tumbleweeds, guided by light with greater controllability than random natural wind. In the meantime, it executed cyclic reciprocal rolling in response to the circadian variation of sunlight direction and performed self-sustained underwater wiring for potential applications. Last, the weaving method and Twirlbot structural design, coupled with photo-driven omnidirectional rolling, could be extended to other material systems, albeit with potential trade-offs in locomotive speed and some functionalities. Notably, highly cost-effective commercial options, such as polypropylene (PP)/cellulose with black marker, offer excellent scalability and substantially reduced cost, over an order of magnitude lower than existing autonomous untethered robot designs. Overall, these features position the multifunctional and multiterrain Twirlbot as a promising advancement in autonomous robotics.

RESULTS

Design rationale for autonomous rolling

The hollow sphere was constructed by weaving six geometrically identical loops, formed from aligned strips (Fig. 1C), which were further divided into two groups: one closed loop (blue) and the other five physically interlaced strips (Fig. 1D and fig. S1 in Detailed Methods 1.1). In the interlaced group, each strip crossed over all remaining four, forming four overlapping nodes. Notably, it was essential to ensure that each intersection followed an alternating over-under relationship with its adjacent ones so that each loop remained independent yet interlaced to provide mutual structural support (*22*). Exemplified by the purple strip (Fig. 1D), it sequentially passed through the orange, gray, red, and green strips from left to right horizontally. Specifically, it lay above the first (orange) and third (red) strips while it passed beneath the second (gray) and fourth (green) strips, which generated an alternating pattern of over-and-under positions, and thereby resulted in a mutually supportive plane. Next, the individual closed loop (blue) sequentially passed through the five outermost intersections of the previously formed plane, constructing a self-supporting hemispherical structure (Fig. 1E). Last, by connecting the corresponding ends of each of the five strips, a centrosymmetric tumbleweed-like structure of Twirlbot was assembled (Fig. 1F). Therefore, each strip was

physically interlaced with the others without any chemical bonding or adhesion that could hinder deformation continuity and was fabricated based on an active/passive bilayer (Fig. 1G). To achieve pronounced reversible deformation, we selected a LCE doped with an efficient photothermal nanoparticle, candle soot (CS) (fig. S6), for the outer active layer and constructed the inner layer from passive PDMS (*12*, *15*, *24*). Meanwhile, a designed lateral misalignment (matching the width at 2.5 mm) between the two layers was introduced to enhance interfacial adhesion within the bilayer, ensuring a seamless loop closure and avoiding overlap at the connecting region.

With such a bilayer sphere (Fig. 1H), collimated light illumination from the right side heated the exposed region of the bottom outer LCE layer, causing thermal-induced contraction (fig. S7). As the local temperature increased, the resulting deformation was amplified, which reduced the support area and caused a leftward shift of the right support point (purple point), thereby enhancing the total moment (Fig. 1I and Supplementary Text 2.1). When the total moment exceeded the stabilizing limit set by the decreasing contact area with the substrate, Twirlbot fell over to regain stability (Fig. 1J and fig. S8) (*19*). At this moment, the previously irradiated region was no longer exposed to light, resulting in rapid cooling for shape recovery and a new contact surface for the restoration of the total moment (Fig. 1K), thereby completing one fundamental step/cycle in the rolling process. Simultaneously, the new region facing the constant incident light became irradiated, which triggered the next cycle for self-sustained autonomous rolling.

Governing parameters of rolling behavior

By tracking the behavior of Twirlbot, its continuous rolling could be considered as successive steps of deformation-falling-recovery driven by the self-shadowing mechanism (Fig. 2A and movie S1) (*10*, *25*). During the recovery process, the passive PDMS rapidly released the elastic energy accumulated during the photothermal deformation process, thereby facilitating the shape recovery (*15*, *26*). Consequently, the recovery process occurred much faster than the deformation process and exhibited an overshoot beyond the equilibrium state, followed by a damped return to equilibrium (Fig. 2B) (*27*). Meanwhile, infrared (IR) visualization revealed that the movement of Twirlbot at the peak temperature during each falling action was essential to generate the highest displacement velocity, which enabled continuous pulsed rolling (Fig. 2C and fig. S9).

However, structure with same geometries, specifically in diameter and strip width, made from LCE monolayers, PDMS monolayers, or LCE/paper bilayers was unable to achieve self-continuous motion due to various reasons (fig. S10): (i) For pure LCE Twirlbot, the recovery time of the active layer was longer than the deforming time, preventing complete recovery before the next cycle and ultimately leading to the structure collapse step by step; (ii) for pure PDMS Twirlbot, the material was unable to respond to stimuli; and (iii) for LCE/paper Twirlbot, the deformability of the passive layer was insufficient, which restricted the active layer from generating adequate deformation before it was burned at high temperature. These phenomena indicated that the interplay between active and passive layers governed both the deformation and recovery performance, which played a decisive role in achieving autonomous rolling.

Building upon this conclusion and to further investigate the rolling behavior of the entire structure, we introduced two geometric parameters associated with each bilayer loop, the thickness ratio of passive to active layer (d_{PDMS}/d_{LCE}) and the width of each bilayer strip, while keeping the length of each strip fixed at 60 mm. These two parameters would substantially influence the deformability at the knots, each of which was constructed by three intersecting strips (fig. S4), and thus determined the overall photo-driven behavior of Twirlbot. Under different parameter combinations, Twirlbot exhibited three distinct modes of motion (Fig. 2D and fig. S11): (i) It collapsed after completing a limited number of cycles when the proportion of passive layer (i.e., d_{PDMS}/d_{LCE}) was low and the width was narrow, indicating sufficient deformability but limited recovery capability; (ii) self-sustained continuous rolling was achieved with appropriate d_{PDMS}/d_{LCE} and width when the knots had both excellent deformability and recovery performance; and (iii) it remained stationary when d_{PDMS}/d_{LCE} or width was too large, as it only had adequate recovery capability without sufficient actuation performance.

The reason lies in the bending stiffness of each bilayer strip and the interlaced architecture. For each bilayer strip, an increased d_{PDMS}/d_{LCE} reflected a higher fraction of the passive layer, which increased the bending stiffness and therefore reduced photoinduced bending performance (fig. S12). On the other hand, both d_{PDMS}/d_{LCE} and strip width demonstrated similar effects in suppressing knot mobility, as larger values of either parameter amplified the effective compression between intersecting strips (fig. S5 in Supplementary Text 2.2). This reduced mobility led to a corresponding drop in rolling speed, primarily due to the decreased step frequency while the step length remained comparable (Fig. 2, E and F, and fig. S13). In the meantime, such increases facilitated the accumulation of elastic energy and promoted its release, which was beneficial for the shape recovery during rolling. The reason was elucidated through the compression tests (Fig. 2G). For example, when compressed to the same extent (e.g., 50% strain), the hollow spherical structure with higher d_{PDMS}/d_{LCE} or width generated greater compressive force, an indicator of deformation resistance. Next, when the compressive force was removed and the structure recovered naturally, it was observed that increasing d_{PDMS}/d_{LCE} or width enhanced the recovery rate (fig. S14). Specifically, the d_{PDMS}/d_{LCE} influenced the deformability of the knots along the thickness direction, where a thicker passive layer increased the effective modulus (*28*) and reduced length variation of the bilayer, which, in turn, elevated the temperature to trigger bending and thereby resulted in a higher level of accumulated elastic energy (fig. S15).

Meanwhile, to further illustrate our observations, a multiphysics finite element analysis (FEA) model using COMSOL Multiphysics was developed to simulate the behavior of a knot structure. This structure was composed of three interwoven bilayer strips, each consisting of an active LCE layer and a passive PDMS layer. The strips were fixed at both ends, initially forming a convex spherical node (fig. S4 and Supplementary Text 2.2). We assumed that the overall structure of Twirlbot remained constant, with its falling being triggered once the irradiated knot reached a predefined deformation displacement (d). The applied photothermal temperature profile, derived from IR camera measurements, initially increased from room temperature to induce a concave deformation with a displacement of 2 mm, followed by gradual cooling to restore the original shape (Fig. 2H, top). This simulation enabled us to evaluate how variations in the d_{PDMS}/d_{LCE} ratio and strip width influenced the knot's stress distribution and kinematic behavior during each irradiated cycle. For example, with d_{PDMS}/d_{LCE} increased, the resistance to deformation in the knot enhanced accordingly, which required a longer irradiation time to reach a higher actuation temperature (fig. S16). This change subsequently caused a higher

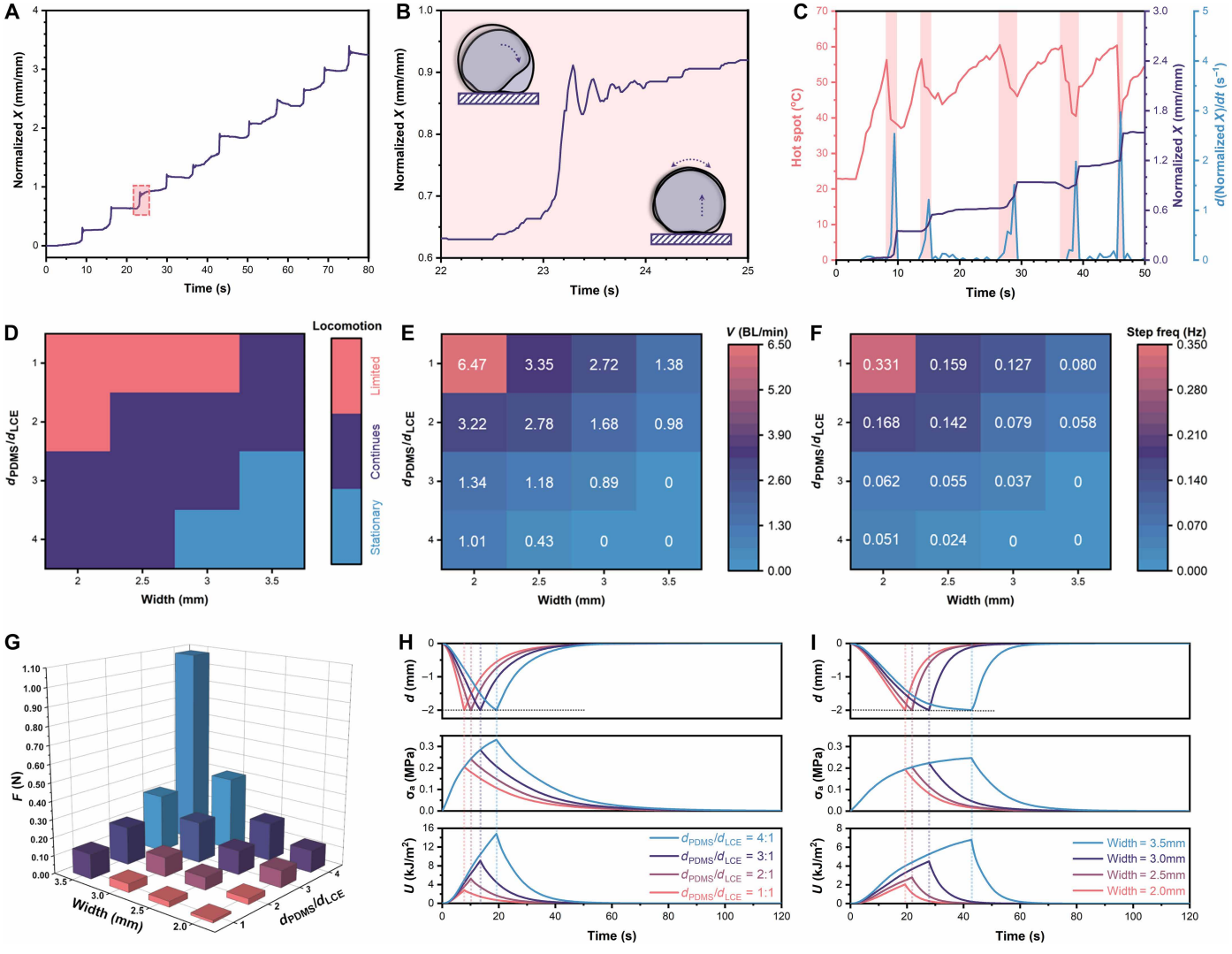

Fig. 2. Rolling process and influence of geometric parameters. (**A**) Displacement profile during the continuous rolling process and (**B**) zoom-in view of a single rolling cycle, where *X* denotes the horizontal displacement of the Twirlbot, normalized by its diameter. (**C**) Relationship among temperature, displacement, and velocity during self-sustained rolling. (**D**) Effect of varying d_{PDMS}/d_{LCE} and widths in determining the three motion modes of Twirlbot under constant light with an intensity of ~600 mW/cm^2: limited-cycle rolling, continuous rolling, and stationary. (**E**) Mapping of rolling speed and (**F**) step frequency (i.e., falling frequency) for Twirlbot to the same parameter variations under constant light with an intensity of ~600 mW/cm^2, with BL representing body length. (**G**) Compressive force measured at 50% strain for Twirlbot with varying d_{PDMS}/d_{LCE} and widths. (**H**) Modeling results showing the light-induced deformation at each knot for different d_{PDMS}/d_{LCE} (width fixed at 2.5 mm) and (**I**) different widths (d_{PDMS}/d_{LCE} fixed at 2), where *d*, σ_a, and *U* represent actuation strain, actuation stress, and elastic energy density, respectively.

actuation stress (σ_a) and elastic energy density (*U*) (Fig. 2H and Supplementary Text 2.3). It was observed that, when d_{PDMS}/d_{LCE} was 1:1, the heating rate exceeded the cooling rate, which was the reason for undissipated heat accumulation and the gradual collapse of samples during repeated cycles. As d_{PDMS}/d_{LCE} further increased, the temperature difference between the triggered region and the ambient environment increased, resulting in an enhanced cooling speed. This, in turn, promoted the cooling-induced recovery and energy release in the knot and, ultimately, gave rise to the self-continuous rolling of Twirlbot. A similar trend was observed across groups with varying strip widths (Fig. 2I). As the width increased, samples with the same d_{PDMS}/d_{LCE} required longer irradiation time, which led to greater energy accumulation, elevated triggering temperature, and enhanced σ_a. In addition, the thermal effective modulus (E_{the}), defined as the ratio of thermal stress to effective strain, characterized the overall stiffness of the composite structure under internal stresses induced by thermal expansion or contraction, thereby quantifying its resistance to deformation during the photothermal cycle (Supplementary Text 2.4). The calculated trend of E_{the} was consistent with the experimentally measured compression results (Fig. 2G), which showed that both increased d_{PDMS}/d_{LCE} and width contributed to a higher modulus (fig. S17).

In addition, the strip number fundamentally determined the structural stability of the Twirlbot (table S1). When the strip number was less than or equal to 3, a closed surface could not be formed, and the architecture disassembled under illumination. Although the deformation of the individual strip could be recovered, the overall structure could not reset for sustained motion. Increasing the strip

number to four or five introduced additional intersection knots; however, their sparse distribution on the spherical surface still resulted in large openings and insufficient stiffness, leading to irreversible collapse during irradiation. Only when the strip number reached 6, corresponding to 20 intersecting knots, did the architecture achieve sufficient structural stiffness and recovery capability to sustain continuous deformation-recovery cycles. On the other hand, strip length also influenced the rolling performance. Increasing the strip length alone reduced the overall structural stiffness, rendering the architecture insufficient to sustain continuous motion. In contrast, proportionally scaled-up Twirlbots, in which the width, length, and thicknesses of both the LCE and PDMS layers of each bilayer were increased simultaneously, could maintain self-sustained rolling performance (fig. S18 and movie S2). However, their step frequency decreased under the same light intensity because the thicker PDMS layer introduced greater deformation resistance and slower thermal diffusion. Meanwhile, because the illumination area remained identical and consistently covered the bottom half of the Twirlbot, the deformation region and the resulting step length changed marginally. As a result, the normalized rolling speed gradually decreased with increasing Twirlbot size.

In addition to the geometric parameters, the constant light, serving as the sole energy input, played a critical role in governing the rolling behavior. Herein, the optimal spot width should cover the entire width of Twirlbot to prevent too narrow illumination from passing through structural gaps and to avoid nonuniform irradiation on the outer surface (fig. S19). Thus, a laser was used for testing, with its beam width spanning the full diameter of the Twirlbot and its height W set to the radius of the Twirlbot (subsequent experiments were conducted with $d_{PDMS}/d_{LCE} = 2{:}1$, strip width of 2.5 mm, strip length of 60 mm, with a diameter of ~18 mm unless otherwise specified) (Fig. 3A). Therefore, the distance Y between the bottom of the laser spot and the ground determined the irradiation area. As Y decreased from 0 to negative values, the irradiation area gradually diminished, resulting in a decreased deformation area accordingly. Under such conditions, the frequency did not vary notably, and the decreasing Y rendered a proportional decrease in step length and the corresponding rolling velocity (Fig. 3B, left). On the other hand, an increase in Y within the range greater than 0 altered the illumination position without affecting the irradiation area. Consequently, the deformation range and step length remained unchanged, whereas the frequency of the total moment change was decreased accordingly. When normalized Y exceeded $^1/_4$, the center of the illumination position shifted above the center of the sphere, which resulted in insufficient deformation of the bottom hemisphere to reduce the supporting area and generate a sufficient total moment for falling over, and, thus, no displacement occurred (Fig. 3B, right). Similar trends were observed in Twirlbot with different strip widths, where $Y = 0$ consistently yielded the maximum rolling speed. The different widths primarily affected the time for energy accumulation to produce sufficient deformation, i.e., the frequency; the constant step length was due to the same irradiation area for the identical deformation range (fig. S20). In addition, when the irradiated area remained constant, an increase in light intensity only promoted the accumulation of elastic energy for deformation, which, in turn, proportionally facilitated the rolling velocity by raising the frequency (Fig. 3C).

In conclusion, the rolling velocity of Twirlbot, governed by step length and frequency, can be effectively modulated by manipulating the light in three aspects: (i) Increasing the illumination area enhances deformation, thus increasing step length, regardless of structural parameters (e.g., strip width); (ii) adjusting the illumination position regulates the total moment for frequency variation, with no displacement occurring if the light center is above the center of the spherical structure; and (iii) increasing light intensity proportionally elevates actuation frequency, leading to higher rolling speed.

Embodied multifunctionality

To explore the functionality of Twirlbot, we first demonstrated that it was able to perform autonomous rolling and ascend/descend a vertical height (H) on inclined glass surfaces with tilting angles ranging from 6° to −6°, providing sufficient friction to prevent it from falling (Fig. 3D and movie S3) (*29*). Due to the gravity, the rolling speed was calculated to be inversely proportional to the inclination angle (fig. S21). Moreover, the material combination of LCE and PDMS endowed Twirlbot with excellent robustness. The individual bilayer strip exhibited minimal fatigue in both actuation stress and adhesion over 100 actuation cycles (fig. S22), resulting in negligible deterioration in deformation capability and near-complete recovery of the Twirlbot with no residual stress after repeated actuation cycling (Fig. 3E). As a result, Twirlbot retained its spherical architecture for rolling even after being trampled (fig. S23 and movie S4). Meanwhile, the strong elastic recovery of the strip allowed for easy stretching to insert cargo into Twirlbot's body. The cargo size substantially influenced the rolling speed (Fig. 3F and movie S5). When the cargo diameter approached that of Twirlbot (such as tissue paper shown in fig. S24A), its deformation capability was constrained by the contact force between the cargo and the inner wall under full-volume conditions. Such forces increased with the mass of the cargo, leading to a corresponding decrease in the overall rolling speed. In contrast, for cargo with a diameter smaller than that of Twirlbot (such as aluminum foil shown in fig. S24B), Twirlbot was able to carry loads exceeding its own mass while maintaining a certain speed before its operational limit. Moreover, this cargo-carrying capability could be extended to inclined planes, although its transport performance gradually decreased as the inclination angle increased (fig. S25 and movie S5).

Owing to its symmetric structure, Twirlbot was capable of achieving omnidirectional, self-sustained rolling toward the light. When it passed through the central region, the manual adjustment of the incident light direction did not affect the Twirlbot's ability to consistently reorient toward the light source (movie S6). The results showed that Twirlbot exhibited a negligible turning radius and could achieve continuous 360° azimuthal movement (Fig. 3G). Consequently, the Twirlbot enabled arbitrarily reconfigurable trajectories guided by a human-controlled incident light source, allowing programmable paths such as the letter "n" (Fig. 3H). Notably, this omnidirectional rolling was achieved without compromising rolling speed, representing an important advancement toward the development of autonomous soft robots (fig. S26 and table S2). Moreover, the omnidirectional behavior enabled positive phototaxis, which served as an intelligent behavior observed in living organisms such as *Euglena* and *Navicula* (*30*). Specifically, when encountering a second and stronger light, the Twirlbot spontaneously corrected its rolling direction through the larger photoinduced deformation, exhibiting positive phototaxis (Fig. 3I and movie S7). Furthermore, this light-guided sustained rolling can be maintained even under crosswinds with a velocity of 2.9 m/s, corresponding to a Beaufort scale of 2 (light breeze) (fig. S27 and movie S8). By contrast, under stronger wind conditions, the Twirlbot lost directional control and transitioned to a passive tumbleweed-like

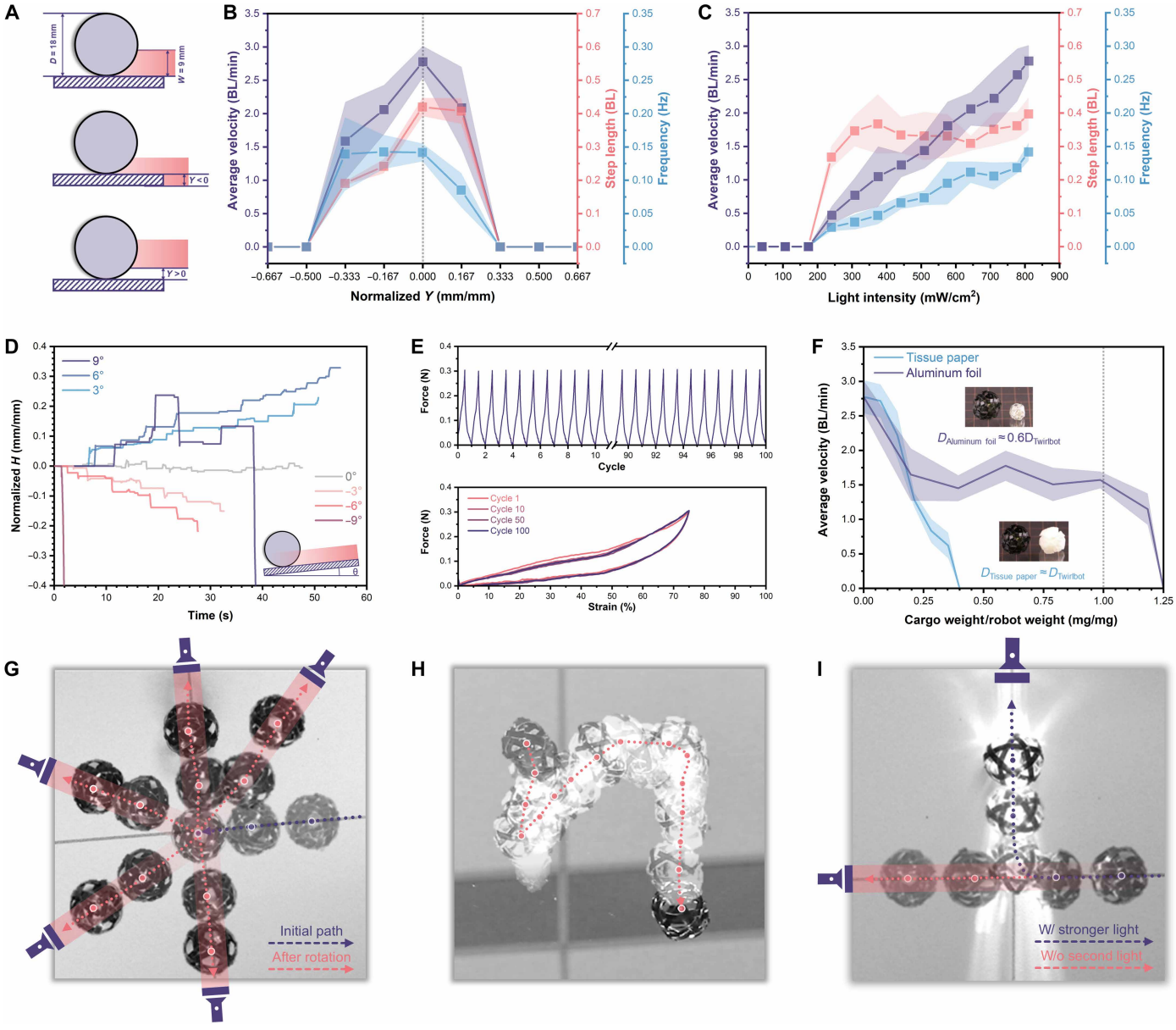

Fig. 3. Autonomous rolling controlled by light and multifunctionality of Twirlbot. (**A**) Schematic illustration and (**B**) rolling performance under constant light from different irradiation positions, where *Y* is defined as the distance between the lowest point of the laser spot and the substrate surface, normalized by the diameter/body length (BL) of the Twirlbot. (**C**) Rolling performance under varying light intensities. (**D**) Rolling behavior on inclined planes, where *H* denotes the vertical height ascended by the Twirlbot, normalized by its diameter. (**E**) Cyclic performance of elastic deformation. (**F**) Cargo transportation capability, with BL representing body length. (**G**) Omnidirectional turning behavior. (**H**) Light-guided rolling with an arbitrarily reconfigurable trajectory. (**I**) Self-correction for positive phototaxis.

rolling behavior. These multifunctional characteristics, integrated within a single-component system, underscore Twirlbot's promising potential for real-world applications.

Potential for real-world applications

In real-world environments, surfaces are often complex and may include obstacles. To assess the terrain adaptability of Twirlbot, we evaluated its rolling performance across a variety of surfaces. The results demonstrated that Twirlbot maintained stable locomotion over a broad range of surface roughness values (R_a from 10^{-3} to 10^4 μm), including paper, metal, and acrylic board, glass (Fig. 4A, fig. S28, and movie S9), and even when these surfaces were tilted (fig. S29). Furthermore, due to its crawling capability and inherent elasticity, Twirlbot was able to effectively roll over the obstacles with a maximum height equal to 0.11 of its diameter (fig. S30). Meanwhile, the scaled-up Twirlbot could overcome obstacles of larger absolute dimensions. Thus, small natural obstacles such as gravel and wood debris that were within its deformation range would not impede its self-sustained locomotion (fig. S31). As a result, it successfully navigated across complex real-world terrains, such as gravel, sand, leaves, and soil in forest trails.

In nature, the tumbleweed rolls passively under random wind and relies on physical contacts with the ground and friction to achieve

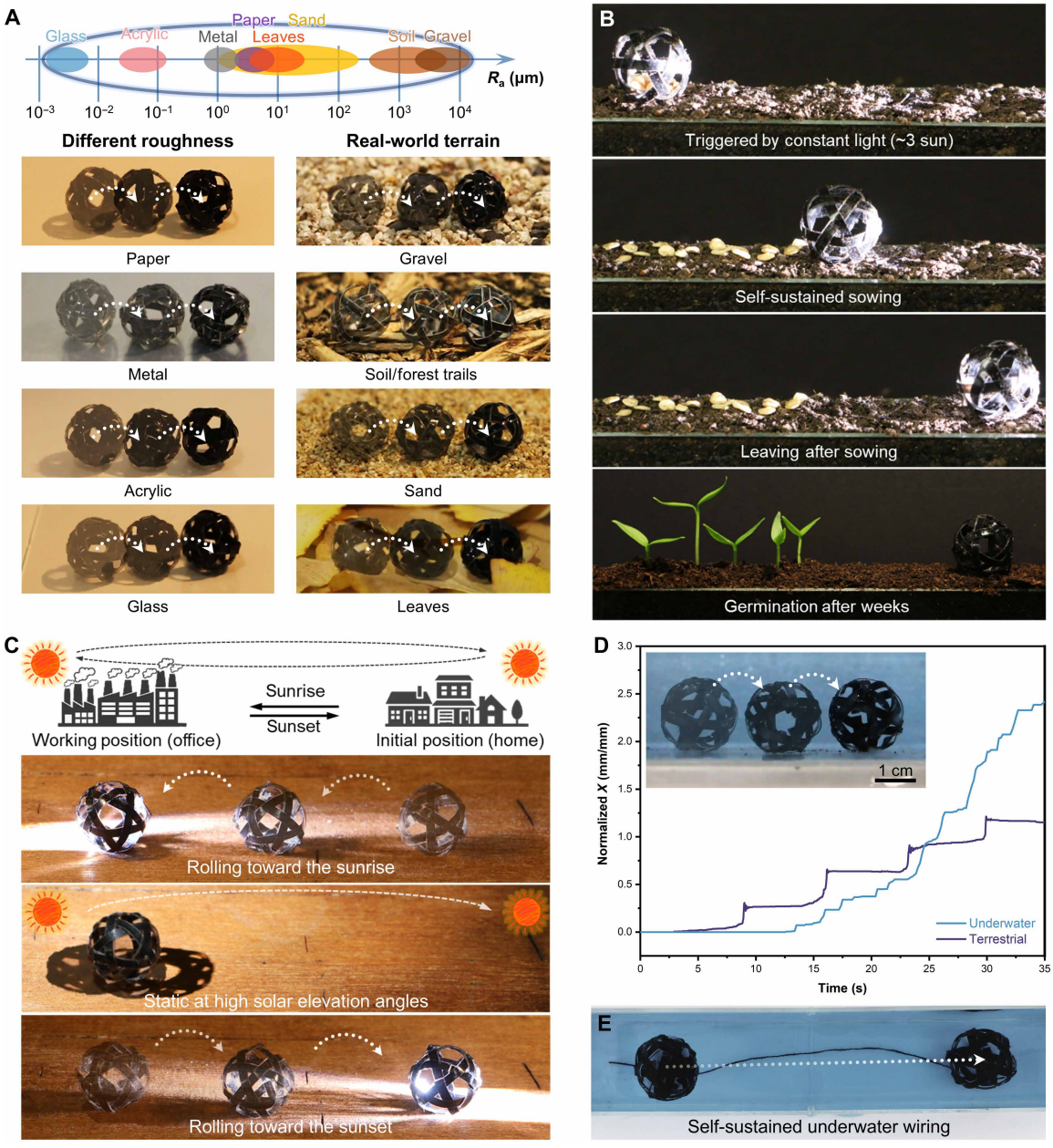

Fig. 4. Potential real-world applications of Twirlbot. (**A**) Self-sustained rolling across multiple terrains with adaptation to a broad range of surface roughness levels. (**B**) Autonomous selective seed-sowing behavior. (**C**) Autonomous daily commuting vehicle with reversible rolling between sunrise and sunset. (**D**) Underwater locomotion and (**E**) self-sustained wiring.

seed detachment. In addition to such passive sowing, Twirlbot was further capable of actively pursuing sunlight to controllably disperse seeds from its internal cavity, triggered by vibrations generated during the falling-over motion (movie S10). This capability enabled self-sustained and orderly sowing of a substantial quantity of seeds, 179.9 mg of bell pepper seeds carried by the Twirlbot with a mass of 354.6 mg, along the illuminated path within a few minutes (Fig. 4B). When the sowing process was completed, Twirlbot autonomously departed from the site, avoiding interference with the natural germination and growth of the seeds. This fully autonomous operation demonstrated the feasibility of autonomous seed dispersal, extending beyond the seed quantity and distance presented in the current demonstration. Theoretically, scaling up the Twirlbot and ensuring continuous, unobstructed light irradiation would enable the transport of a seed payload exceeding half of the Twirlbot's body weight across unlimited distances until all seeds are fully dispersed.

Furthermore, by placing concentrator lenses horizontally on both sides (fig. S2), Twirlbot was able to harness the periodic movement of sunlight and functioned as an autonomous daily commuting vehicle with reversible locomotion (Fig. 4C and movie S11). At sunrise, sunlight passed through the left lens, and the focused beam (with an

intensity of about three times that of ambient sunlight) activated the Twirlbot's phototropic response, which triggered autonomous rolling from the initial position (right) to a designated working position (left). Once the solar elevation angle increased beyond the focal range of the lens, the light intensity and incidence position on the Twirlbot surface became insufficient to sustain locomotion, leaving it stationary at the designated location for potential resupply or reloading. As the day progressed toward sunset, the focused light passing through the right-side lens reactivated the Twirlbot and enabled it to autonomously return to its initial position. This was achieved owing to the symmetric positioning of the lenses and comparable illumination duration, thereby completing the reciprocal cycle. With both short-duration (minute-scale) autonomous sowing and daily reciprocal movement successfully demonstrated, Twirlbot can be considered a promising candidate for sunlight-fueled, autonomous agricultural robots in real-world environments.

Given the stability of LCE and PDMS in water, the application scope of Twirlbot could be extended to aquatic environments, where it also exhibited self-sustained rolling under constant irradiation (Fig. 4D and movie S12). Due to the higher thermal conductivity of water, Twirlbot required a longer duration to accumulate sufficient photothermal energy to initiate locomotion. However, this enhanced thermal conductivity also facilitated faster recovery after each deformation process and generated greater thermal gradients between the irradiated and nonirradiated regions, which led to more effective asymmetric deformation. In addition, buoyancy partially supported the structure and reduced ground friction during rolling compared with the identical terrain in air, enabling the same Twirlbot to achieve more than twice the speed observed on land ($v_{underwater}$ = 5.69 BL/min; v_{land} = 2.78 BL/min). This multienvironmental adaptability broadens the application potential of Twirlbot for controllable underwater release or deployment, such as self-sustained underwater wiring that extends its functionality beyond locomotion (Fig. 4E and fig. S32).

Material extension toward ultralow-cost system

The structural design of Twirlbot is not limited to LCE-driven systems. As previously discussed, as long as the fabrication approach is consistent and the active/passive bilayer strips exhibit appropriate deformation and recovery capabilities, a wide range of material combinations—including even the most inexpensive, commercially available materials—can be used to develop Twirlbots. For instance, we selected cellulose weighing paper and adhesive polypropylene (PP) tape to directly construct the bilayer structure (Fig. 5A and fig. S33A), which has been proven to exhibit appreciable reversible macroscopic deformation under modest temperature variations (*31*). Meanwhile, a black marker was used to paint the cellulose paper black for photothermal conversion as a substitute for embedded CS (fig. S33B). As a bilayer strip, the PP layer expanded while the cellulose layer underwent contraction under moderate heating (<65°C) (fig. S33C), similar to the thermal response observed in PDMS and LCE bilayers (fig. S10). This mismatch induced asymmetric deformation of each PP/cellulose bilayer at the locally heated region, which resulted in a bending angle that decreased from 180° to 90° at 48°C and further to 30° at 69°C (Fig. 5B).

Following the same fabrication method, PP/cellulose-based Twirlbots were assembled with each bilayer intersecting the other five, exhibiting scalable diameters from ~8.37 mm to ~9.63 cm, which could be easily extended to larger ranges if permitted by larger papers and wider tapes (Fig. 5C). Consequently, they effectively converted constant light irradiation into a directional heat to power continuous rolling locomotion and relevant functional behaviors like climbing, trampling resistance, cargo transport, omnidirectional locomotion, and self-correction (Fig. 5D and fig. S34). Admittedly, the rolling velocity, step frequency, and step length of the PP/cellulose Twirlbot were relatively lower than those of the LCE/PDMS counterpart (fig. S33D), primarily due to the smaller heat-induced strain difference and the lower maximum delamination temperature of the PP/cellulose bilayer. Meanwhile, this material system compromised

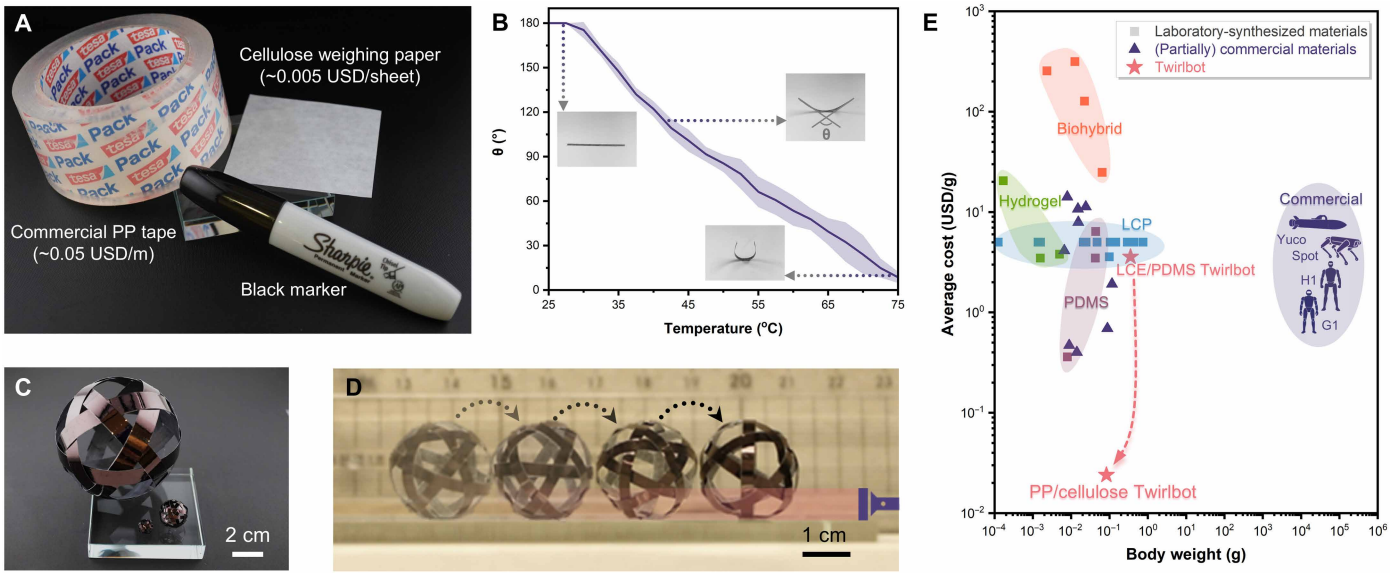

Fig. 5. Twirlbot constructed from commercial materials. (**A**) Raw materials used for preparing bilayer strips. (**B**) Thermal response of the PP/cellulose bilayer. (**C**) Fabricated PP/cellulose Twirlbots with scalable geometry. (**D**) Continuous rolling under constant irradiation with an intensity of ~600 mW/cm^2. (**E**) Cost comparison of untethered autonomous robots, with H1 and G1 indicating the humanoid robot models developed by Unitree (*1*, *13*–*15*, *25*, *39*–*68*).

some of the additional functionalities, such as climbing capability, load capacity, underwater locomotion, and wind resistance (fig. S35). Nevertheless, these results demonstrated that the fabrication method and structural design of Twirlbot could be extended to a wider range of material systems beyond the laboratory-synthesized materials, including commercially available options that are both cost-effective and accessible to nonspecialists. Specifically, the average cost of each PP/cellulose Twirlbot could be reduced to the order of 10^{-3} USD (~0.002 USD per 18-mm-diameter unit) based on the average material cost of ~0.02 USD/g, which is at least one order of magnitude lower than that of existing untethered robot designs (Fig. 5E and table S3). This distinct cost advantage, together with scalability from millimeter to decimeter level, offers a promising route toward scalable manufacturing and real-world deployment, particularly in light of its light-guided autonomous omnidirectional locomotion and multifunctional capabilities.

DISCUSSION

We proposed a Twirlbot, constructed from six interlaced closed loops using the weaving-based fabrication method. The photoactive/passive bilayer architecture governed both deformability and recovery ability, enabling self-continuous rolling under constant irradiation, as supported by our FEA modeling. Owing to its centrosymmetric hollow sphere structure, Twirlbot exhibited the multifunctionality of rolling capabilities, such as climbing, trampling-resistance, load-carrying, and positive phototaxis, all enabled by its omnidirectional performance. Therefore, Twirlbot was capable of adapting to various terrains with diverse surface roughness and obstacles, as well as operating effectively under underwater conditions. These features enabled Twirlbot to function as a self-sustained seeder under constant sunlight, an autonomous commuting vehicle between sunrise and sunset, and an underwater autonomous cable-laying robot. Furthermore, the structural design and fabrication strategy of Twirlbot were scalable and compatible with diverse material combinations, including commercial materials, enabling ultralow production cost with broad generality.

Although the material system that we tested still requires a convex lens to focus sunlight, rapidly advancing material systems (e.g., dynamic bonding-based bilayer) offer promising potential to enable self-sustained motion driven by ambient heat or human body temperature (*32*). Such developments would substantially lower the activation threshold of this architecture and enhance its feasibility for real-world applications, including operation under diurnal variations in sunlight orientation or reduced irradiance on cloudy days. At present, the Twirlbot composed of six strips exhibits a zigzag trajectory due to surface gaps, whereas increasing the number of strips is expected to favor straighter motion. Theoretically, this interweaving strategy can be extended to more-strip architectures by replacing the single closed loop (blue in Fig. 1D) with one or two additional groups of five interlaced strips, forming 10- or 15-strip structures that more closely approximate a perfect sphere for enhanced rolling performance (fig. S36 and Supplementary Text 2.5).

In general, all of these features were achieved within a single-component system, which opened the way for the next generation of untethered, autonomous, energy-sustainable, and cost-effective robots, particularly in the fields of robotics and agriculture.

MATERIALS AND METHODS

Materials

Diacrylate liquid crystal monomer 2-methyl-1,4-phenylene bis(4-(3-(acryloyloxy)propoxy)benzoate) (RM257) was obtained from Shijiazhuang Sdyano Fine Chemical Co. Ltd. Pentaerythritol tetrakis (3-mercaptopropionate) (PETMP), 2,2′-(ethylenedioxy)diethanethiol (EDDET), 1,6-hexanedithiol (HDT), I-2959, dipropylamine (DPA), tetraethyl orthosilicate (TEOS), ammonia solution (30%), hexane, and toluene were sourced from Sigma-Aldrich. Sylgard 184 PDMS kits were purchased from Ellsworth. In addition, silicone glue (Permatex 82194), candles (Missyo), PP tape (TESA transparent 60 m by 55 mm), cellulose weighing paper [VWR; 2.4 inches (6.096 cm) by 2.4 inches (6.096 cm)], and black markers (Sharpie) were acquired from Amazon. All chemicals were used as received without further purification.

Material preparation

CS was used as the photothermal agent, collected by holding an aluminum foil above a candle flame and then scraping off the soot with a clean blade (*33*). The LCE/CS preparation followed our previously developed procedure involving a two-step thiol-acrylate click reaction (*15*, *34*). First, 250 mg of RM257 and 2.5 mg of I-2959 were dissolved in 77.5 mg of toluene at 80°C. The 1.6 mg of CS was then uniformly dispersed in the mixture through sonication for a minimum of 2 min. Afterward, 9.6 mg of PETMP, 38.4 mg of HDT, and 34 μl of diluted DPA solution (2 wt % in toluene) were added to the 235 mg mixture in sequence at 80°C with vigorous stirring. After a 3-min reaction, the mixture was cast between two tape-covered glass slides with a spacer and cured at 60°C for at least 48 hours. The resulting LCE film was then carefully peeled from the mold, uniaxially stretched to 100% strain, and subjected to photocrosslinking under an ultraviolet (UV) lamp (UVGO, 365 nm) at an intensity of 35 mW/cm^2 for 2 hours on each side. The PDMS film was prepared by mixing the base and curing agent in a 5:1 ratio. After vacuum defoaming for at least 5 min, the mixture was poured into glass molds with predefined spacers and cured overnight at 80°C, followed by careful demolding.

Fabrication of the bilayer strip

The prepared LCE and PDMS monolayers were pretreated to enhance adhesion before assembly. First, the LCE film was cut to dimensions of 25 mm by 2.5 mm by 120 μm and immersed in ethanol overnight as the surface treatment. Simultaneously, the PDMS film was cut to the same length and width dimensions, with the thickness according to the design (120, 240, 360, and 480 μm), and washed with hexane. Both the cleaned LCE and PDMS monolayers were treated with oxygen plasma for 3 min, followed by the deposition of a thin silica coating through chemical vapor deposition using TEOS and ammonia solution for 6 hours and 90 min, respectively. Next, the LCE and PDMS films were then assembled into a bilayer strip using silicone glue (10 wt % in hexane) (*11*). After assembly, the bilayer strip was placed in an oven to evaporate the hexane and cure the glue at 60°C for at least 3 days. PP/cellulose bilayer strips were first prepared by directly attaching commercial PP tape onto the surface of cellulose weighing paper. A glass slide was used to remove air bubbles and ensure sufficient adhesion and uniform surface. The exposed side of the cellulose paper was then uniformly painted by a black marker and dried in air. The PP/cellulose bilayer was subsequently cut into strips of the desired length and width for use in Twirlbot fabrication (detailed in the Supplementary Materials).

Setup for rolling tests

The setup for rolling tests consists of an acrylic board and an 808-nm laser (LSR808NL, DPSS Laser) positioned in parallel. The rectangular light spot was expanded using a horizontally placed diffuser to cover the entire diameter of the Twirlbot. The safe operating window was from 240 to 810 mW/cm^2, as the LCE/PDMS bilayer began to delaminate when the light intensity reached 860 mW/cm^2.

All locomotion was captured and recorded by a camera (EOS 70D, Canon) at 60 fps for at least five rolling cycles per trial. The omnidirectional turning tests were recorded by a fixed overhead camera, with a fixed laser and a rotating stage used to tune the incident angle between the light and the Twirlbot, whereas arbitrarily reconfigurable trajectories were achieved using a handheld solar simulator.

Each parameter was tested at least three times to calculate the average value. The standard deviation is indicated by the colored pattern beneath each data point. The software Tracker was used to track selected points for positions and displacements, which were then used to calculate the frequency and speed of locomotion.

Mechanical characterizations

For the compression test, each Twirlbot was characterized using a dynamic mechanical analyzer (DMA850, TA Instruments) equipped with a disk compression clamp and subjected to a preload of 0.01 N. The compressive force was recorded at 50% strain (i.e., half of the diameter) under a strain rate of 10%/min at room temperature. Three specimens were tested for each formulation to ensure reproducibility.

The adhesion force was measured by peel testing using the same dynamic mechanical analyzer (DMA850, TA Instruments) equipped with a rectangular film clamp at room temperature. Two different layers were fixed separately in opposing clamps at a 180° configuration and pulled apart at a rate of 2 mm/min under a preload of 0.01 N.

Cyclic elastic deformation tests of each Twirlbot were performed using a CellScale Univert mechanical tester equipped with a 4.5-N load cell and a compression module. The preload and strain amplitude were set to 0.01 N and 75%, respectively, at room temperature. Each loading cycle comprised a 30-s compression phase followed by a 30-s recovery phase, with no hold time between cycles.

Thermomechanical characterizations

All the samples were annealed at 180°C for 5 min and then cooled to room temperature to eliminate thermal history. The moduli, stresses, and lengths were measured using a dynamic mechanical analyzer (DMA850, TA Instruments) under a preload of 25 kPa, an oscillation frequency of 1 Hz, and a heating rate of 5°C/min.

Differential scanning calorimetry (DSC250, TA Instruments) was conducted to measure the phase transition of LCE and the thermal properties of PDMS. Specifically, a 10 mg sample was sealed in an aluminum pan, heated to 200°C at a rate of 10°C/min, and held for 2 min. The sample was then cooled to 0°C at the same rate of 10°C /min, followed by a second heating ramp to 200°C at 10°C /min.

Cyclic actuation stress tests were performed using an Instron 68SC-1 mechanical tester in isostrain mode, with both ends of the bilayer strip fixed. Actuation was triggered by periodic irradiation from an 808-nm laser at a light intensity of 810 mW/cm^2, with each cycle consisting of 25 s of illumination followed by 25 s of relaxation without irradiation.

Other characterizations

The particle size of the CS was measured by dynamic light scattering using a Zetasizer Pro (Malvern Panalytical). CS particles were dispersed in toluene at a concentration of 0.1 mg/ml before measurement.

Optical images were captured by a microscope (Leica DM5000 B) to offer high-resolution visualization of the LCE/PDMS bilayer. The photothermal process and thermographic images were captured using an IR camera (TiX 580, Fluke) and analyzed with the Fluke Connect software. UV-visible spectra were measured to investigate the absorption or transmittance by a spectrometer (UV-3101PC, Shimadzu).

For the wind-resistance test, wind was generated by a small electric fan (NISSYO.AM F06) positioned directly facing the stage, while a fixed camera was placed above the setup to record the motion. Wind speed was measured using a digital anemometer (BTMETER BT-100), which was set directly facing the fan and positioned adjacent to the stage where the Twirlbot was rolling. Measurements were taken at 2-cm intervals along the airflow direction.

The surface roughness of commercial paper, metal, acrylic, and glass was measured using the surface roughness tester (AMT220), while the roughness of real-world terrain was obtained from literature, including gravel (*35*), soil (*36*), sand (*37*), and leaves (*38*).

Supplementary Materials

The PDF file includes:

Detailed Methods
Supplementary Text
Figs. S1 to S36
Tables S1 to S3
Legends for movies S1 to S12
References

Other Supplementary Material for this manuscript includes the following:

Movies S1 to S12

REFERENCES

1. A. Baumann, A. Sánchez-Ferrer, L. Jacomine, P. Martinoty, V. Le Houerou, F. Ziebert, I. M. Kulić, Motorizing fibres with geometric zero-energy modes. *Nat. Mater.* **17**, 523–527 (2018).
2. S. K. Malu, J. Majumdar, Kinematics, localization and control of differential drive mobile robot. *Glob. J. Res. Eng.* **14**, 1–9 (2014).
3. A. Gfrerrer, Geometry and kinematics of the Mecanum wheel. *Comput. Aided Geom. Des.* **25**, 784–791 (2008).
4. L. Xu, C. Zhu, S. Lamont, X. Zou, Y. Yang, S. Chen, J. Ding, F. J. Vernerey, Programming motion into materials using electricity-driven liquid crystal elastomer actuators. *Soft Robot.* **11**, 464–472 (2024).
5. M. Oevermann, D. Pravecek, G. Jibrail, R. Jangale, R. O. Ambrose, "RoboBall: An all-terrain spherical robot with a pressurized shell," in *2024 IEEE International Conference on Robotics and Automation (ICRA 2024)* (IEEE, 2024), pp. 13502–13508.
6. R. H. Armour, J. F. V. Vincent, Rolling in nature and robotics: A review. *J. Bionic Eng.* **3**, 195–208 (2006).
7. Y. Sugiyama, S. Hirai, Crawling and jumping by a deformable robot. *Int. J. Robot. Res.* **25**, 603–620 (2006).
8. M. Sitti, Physical intelligence as a new paradigm. *Extrem. Mech. Lett.* **46**, 101340 (2021).
9. R. Baines, F. Fish, J. Bongard, R. Kramer-Bottiglio, Robots that evolve on demand. *Nat. Rev. Mater.* **9**, 822–835 (2024).
10. C. Chen, P. Shi, Z. Liu, S. Duan, M. Si, C. Zhang, Y. Du, Y. Yan, T. J. White, R. Kramer-Bottiglio, M. Sitti, T. Iwasaki, X. He, Advancing physical intelligence for autonomous soft robots. *Sci. Robot.* **10**, eads1292 (2025).
11. Y. Zhao, Z. Liu, P. Shi, C. Chen, Y. Alsaid, Y. Yan, X. He, Antagonistic-contracting high-power photo-oscillators for multifunctional actuations. *Nat. Mater.* **24**, 116–124 (2025).
12. C. Chen, Z. Liu, P. Shi, Y. Zhao, S. Duan, Y. Du, Y. Yan, M. Si, T. Iwasaki, X. He, Bio-inspired multimodal soft actuator with environmental self-adaptation. *Nat. Commun.* **16**, 7630 (2025).
13. C. Ahn, K. Li, S. Cai, Light or thermally powered autonomous rolling of an elastomer rod. *ACS Appl. Mater. Interfaces* **10**, 25689–25696 (2018).
14. A. H. Gelebart, D. Jan Mulder, M. Varga, A. Konya, G. Vantomme, E. W. Meijer, R. L. B. Selinger, D. J. Broer, Making waves in a photoactive polymer film. *Nature* **546**, 632–636 (2017).

15. Y. Zhao, Q. Li, Z. Liu, Y. Alsaid, P. Shi, M. Khalid Jawed, X. He, Sunlight-powered self-excited oscillators for sustainable autonomous soft robotics. *Sci. Robot.* **8**, eadf4753 (2023).
16. Y. Zhao, Y. Chi, Y. Hong, Y. Li, S. Yang, J. Yin, Twisting for soft intelligent autonomous robot in unstructured environments. *Proc. Natl. Acad. Sci. U.S.A.* **119**, e2200265119 (2022).
17. Z.-Z. Nie, M. Wang, S. Huang, Z.-Y. Liu, H. Yang, Multimodal self-sustainable autonomous locomotions of light-driven seifert ribbon actuators based on liquid crystal elastomers. *Angew. Chem. Int. Ed.* **62**, e202304081 (2023).
18. X. Lu, S. Guo, X. Tong, H. Xia, Y. Zhao, Tunable photocontrolled motions using stored strain energy in malleable azobenzene liquid crystalline polymer actuators. *Adv. Mater.* **29**, 1606467 (2017).
19. Z. Wang, K. Li, Q. He, S. Cai, A light-powered ultralight tensegrity robot with high deformability and load capacity. *Adv. Mater.* **31**, e1806849 (2019).
20. C. Borger, M. Walsh, J. Scott, S. Powles, Tumbleweeds in the Western Australian cropping system: Seed dispersal characteristics of Salsola australis. *Weed Res.* **47**, 406–414 (2007).
21. J. Sun, W. Liao, Z. Yang, Additive manufacturing of liquid crystal elastomer actuators based on knitting technology. *Adv. Mater.* **35**, 2302706 (2023).
22. G. Kang, Y.-J. Kim, S.-J. Lee, S. K. Kim, D.-Y. Lee, K. Song, Grasping through dynamic weaving with entangled closed loops. *Nat. Commun.* **14**, 4633 (2023).
23. A. Maziz, A. Concas, A. Khaldi, J. Stålhand, N.-K. Persson, E. W. H. Jager, Knitting and weaving artificial muscles. *Sci. Adv.* **3**, e1600327 (2017).
24. P. Shi, C. Chen, Z. Wang, W. Hong, S. Duan, Z. Liu, W. Hou, M. Si, C. W. Zhang, X. He, Air plastron-enabled heat management for enhanced photothermal actuation in underwater soft robots. *Sci. Adv.* **11**, eadx7189 (2025).
25. Y. Zhao, C. Xuan, X. Qian, Y. Alsaid, M. Hua, L. Jin, X. He, Soft phototactic swimmer based on self-sustained hydrogel oscillator. *Sci. Robot.* **4**, eaax7112 (2019).
26. D. Tang, C. Zhang, C. Pan, H. Hu, H. Sun, H. Dai, J. Fu, C. Majidi, P. Zhao, Bistable soft jumper capable of fast response and high takeoff velocity. *Sci. Robot.* **9**, eadm8484 (2024).
27. X. Qian, Y. Zhao, Y. Alsaid, X. Wang, M. Hua, T. Galy, H. Gopalakrishna, Y. Yang, J. Cui, N. Liu, M. Marszewski, L. Pilon, H. Jiang, X. He, Artificial phototropism for omnidirectional tracking and harvesting of light. *Nat. Nanotechnol.* **14**, 1048–1055 (2019).
28. R. M. Christensen, *Mechanics of Composite Materials* (Courier Corporation, 2005).
29. Y.-C. Cheng, H.-C. Lu, X. Lee, H. Zeng, A. Priimagi, Kirigami-based light-induced shape-morphing and locomotion. *Adv. Mater.* **32**, e1906233 (2020).
30. W. Haupt, in *Research in Photobiology*, A. Castellani, Ed. (Springer, 1977), pp. 67–70.
31. M. Amjadi, M. Sitti, High-performance multiresponsive paper actuators. *ACS Nano* **10**, 10202–10210 (2016).
32. M. Si, Z. Liu, C. Chen, W. Lu, D. Liu, P. Shi, Y. Yu, Y. Yan, X. He, T. Chen, Dynamic bonding enabled ambient-driven motors. *Angew. Chem. Int. Ed.* **65**, e18011 (2026).
33. S. Wu, Y. Du, Y. Alsaid, D. Wu, M. Hua, Y. Yan, B. Yao, Y. Ma, X. Zhu, X. He, Superhydrophobic photothermal icephobic surfaces based on candle soot. *Proc. Natl. Acad. Sci. U.S.A.* **117**, 11240–11246 (2020).
34. P. Shi, Y. Zhao, Z. Liu, X. He, Liquid crystal elastomer composite-based photo-oscillator for microrobots. *J. Compos. Mater.* **57**, 633–643 (2023).
35. D. McCarroll, A. Nesje, Rock surface roughness as an indicator of degree of rock surface weathering. *Earth Surf. Process. Landf.* **21**, 963–977 (1996).
36. W. Jester, A. Klik, Soil surface roughness measurement-methods, applicability, and surface representation. *Catena* **64**, 174–192 (2005).
37. A. Martinez, J. D. Frost, The influence of surface roughness form on the strength of sand–structure interfaces. *Géotech. Lett.* **7**, 104–111 (2017).
38. J. Ma, K. Liu, X. Dong, C. Chen, B. Qiu, S. Zhang, Effects of leaf surface roughness and contact angle on in vivo measurement of droplet retention. *Agronomy* **12**, 2228 (2022).
39. M. Oitzman, Unitree Robotics unveils G1 humanoid for $16K, The Robot Report (2024); www.therobotreport.com/unitree-robotics-unveils-g1-humanoid-for-16k/.
40. J. Spires, You can now buy Boston Dynamics' Spot robot for $74,500, DroneDJ (2020); https://dronedj.com/2020/06/16/you-can-now-buy-bostondynamics-spot-robot-for-74500/.
41. Why YUCO is unique, Seaber (2025); https://seaber.fr/why-yuco-auv-is-unique.
42. M. Cheng, H. Zeng, Y. Li, J. Liu, D. Luo, A. Priimagi, Y. J. Liu, Light-fueled polymer film capable of directional crawling, friction-controlled climbing, and self-sustained motion on a human hair. *Adv. Sci.* **9**, e2103090 (2022).
43. Y. Zhao, Y. Hong, F. Qi, Y. Chi, H. Su, J. Yin, Self-sustained snapping drives autonomous dancing and motion in free-standing wavy rings. *Adv. Mater.* **35**, e2207372 (2023).
44. D. S. Kim, Y.-J. Lee, Y. B. Kim, Y. Wang, S. Yang, Autonomous, untethered gait-like synchronization of lobed loops made from liquid crystal elastomer fibers via spontaneous snap-through. *Sci. Adv.* **9**, eadh5107 (2023).
45. Y. Zhao, Y. Hong, Y. Li, F. Qi, H. Qing, H. Su, J. Yin, Physically intelligent autonomous soft robotic maze escaper. *Sci. Adv.* **9**, eadi3254 (2023).
46. A. Kotikian, C. McMahan, E. C. Davidson, J. M. Muhammad, R. D. Weeks, C. Daraio, J. A. Lewis, Untethered soft robotic matter with passive control of shape morphing and propulsion. *Sci. Robot.* **4**, eaax7044 (2019).
47. F. Zhai, Y. Y. Feng, Z. Y. Li, Y. X. Xie, J. Ge, H. Wang, W. Qiu, W. Feng, 4D-printed untethered self-propelling soft robot with tactile perception: Rolling, racing, and exploring. *Matter* **4**, 3313–3326 (2021).
48. F. Qi, Y. Li, Y. Hong, Y. Zhao, H. Qing, J. Yin, Defected twisted ring topology for autonomous periodic flip-spin-orbit soft robot. *Proc. Natl. Acad. Sci. U.S.A.* **121**, e2312680121 (2024).
49. X. Zhou, G. Chen, B. Jin, H. Feng, Z. Chen, M. Fang, B. Yang, R. Xiao, T. Xie, N. Zheng, Multimodal autonomous locomotion of liquid crystal elastomer soft robot. *Adv. Sci.* **11**, e2402358 (2024).
50. Z.-Z. Nie, B. Zuo, M. Wang, S. Huang, X.-M. Chen, Z.-Y. Liu, H. Yang, Light-driven continuous rotating Möbius strip actuators. *Nat. Commun.* **12**, 2334 (2021).
51. L. Yin, T.-F. Miao, X.-X. Cheng, Z.-C. Jiang, X. Tong, W. Zhang, Y. Zhao, Chiral liquid crystalline elastomer for twisting motion without preset alignment of mesogens. *ACS Macro Lett.* **10**, 690–696 (2021).
52. J. J. Wie, M. R. Shankar, T. J. White, Photomotility of polymers. *Nat. Commun.* **7**, 13260 (2016).
53. L. Yang, L. Chang, Y. Hu, M. Huang, Q. Ji, P. Lu, J. Liu, W. Chen, Y. Wu, An autonomous soft actuator with light-driven self-sustained wavelike oscillation for phototactic self-locomotion and power generation. *Adv. Funct. Mater.* **30**, 1908842 (2020).
54. J. Kim, J. Park, S. Yang, J. Baek, B. Kim, S. H. Lee, E.-S. Yoon, K. Chun, S. Park, Establishment of a fabrication method for a long-term actuated hybrid cell robot. *Lab Chip* **7**, 1504–1508 (2007).
55. A. W. Feinberg, A. Feigel, S. S. Shevkoplyas, S. Sheehy, G. M. Whitesides, K. K. Parker, Muscular thin films for building actuators and powering devices. *Science* **317**, 1366–1370 (2007).
56. R. Raman, C. Cvetkovic, S. G. M. Uzel, R. J. Platt, P. Sengupta, R. D. Kamm, R. Bashir, Optogenetic skeletal muscle-powered adaptive biological machines. *Proc. Natl. Acad. Sci. U.S.A.* **113**, 3497–3502 (2016).
57. Y. Kim, Y. Yang, X. Zhang, Z. Li, A. Vázquez-Guardado, I. Park, J. Wang, A. I. Efimov, Z. Dou, Y. Wang, J. Park, H. Luan, X. Ni, Y. S. Kim, J. Baek, J. J. Park, Z. Xie, H. Zhao, M. Gazzola, J. A. Rogers, R. Bashir, Remote control of muscle-driven miniature robots with battery-free wireless optoelectronics. *Sci. Robot.* **8**, eadd1053 (2023).
58. Y. Yang, C. Li, L. C. Palmer, S. I. Stupp, Autonomous hydrogel locomotion regulated by light and electric fields. *Sci. Adv.* **9**, eadi4566 (2023).
59. S. Maeda, Y. Hara, T. Sakai, R. Yoshida, S. Hashimoto, Self-walking gel. *Adv. Mater.* **19**, 3480–3484 (2007).
60. Y. Zhang, H. Jiang, F. Li, Y. Xia, Y. Lei, X. Jin, G. Zhang, H. Li, Graphene oxide based moisture-responsive biomimetic film actuators with nacre-like layered structures. *J. Mater. Chem. A* **5**, 14604–14610 (2017).
61. Z. Zhao, Y. Hwang, Y. Yang, T. Fan, J. Song, S. Suresh, N.-J. Cho, Actuation and locomotion driven by moisture in paper made with natural pollen. *Proc. Natl. Acad. Sci. U.S.A.* **117**, 8711–8718 (2020).
62. B. Shin, J. Ha, M. Lee, K. Park, G. H. Park, T. H. Choi, K.-J. Cho, H.-Y. Kim, Hygrobot: A self-locomotive ratcheted actuator powered by environmental humidity. *Sci. Robot.* **3**, eaar2629 (2018).
63. X. Chen, D. Goodnight, Z. Gao, A. H. Cavusoglu, N. Sabharwal, M. DeLay, A. Driks, O. Sahin, Scaling up nanoscale water-driven energy conversion into evaporation-driven engines and generators. *Nat. Commun.* **6**, 7346 (2015).
64. X. Zhang, Z. Yu, C. Wang, D. Zarrouk, J.-W. T. Seo, J. C. Cheng, A. D. Buchan, K. Takei, Y. Zhao, J. W. Ager, Photoactuators and motors based on carbon nanotubes with selective chirality distributions. *Nat. Commun.* **5**, 2983 (2014).
65. L. Chang, D. Wang, Z. Huang, C. Wang, J. Torop, B. Li, Y. Wang, Y. Hu, A. Aabloo, A versatile ionomer-based soft actuator with multi-stimulus responses, self-sustainable locomotion, and photoelectric conversion. *Adv. Funct. Mater.* **33**, 2212341 (2023).
66. Y. Hu, Q. Ji, M. Huang, L. Chang, C. Zhang, G. Wu, B. Zi, N. Bao, W. Chen, Y. Wu, Light-driven self-oscillating actuators with phototactic locomotion based on black phosphorus heterostructure. *Angew. Chem. Int. Ed.* **60**, 20511–20517 (2021).
67. B. E. Treml, R. N. McKenzie, P. Buskohl, D. Wang, M. Kuhn, L.-S. Tan, R. A. Vaia, Autonomous motility of polymer films. *Adv. Mater.* **30**, 1705616 (2018).
68. X. Yang, L. Chang, N. O. Pérez-Arancibia, An 88-milligram insect-scale autonomous crawling robot driven by a catalytic artificial muscle. *Sci. Robot.* **5**, eaba0015 (2020).
69. E. Akleman, J. Chen, Q. Xing, J. L. Gross, Cyclic plain-weaving on polygonal mesh surfaces with graph rotation systems. *ACM Trans. Graph.* **28**, 1–8 (2009).
70. C. Baek, A. G. Martin, S. Poincloux, T. Chen, P. M. Reis, Smooth triaxial weaving with naturally curved ribbons. *Phys. Rev. Lett.* **127**, 104301 (2021).
71. H. Zeng, O. M. Wani, P. Wasylczyk, A. Priimagi, Light-driven, caterpillar-inspired miniature inching robot. *Macromol. Rapid Commun.* **39**, 1700224 (2018).
72. T. Taniguchi, H. Sugiyama, H. Uekusa, M. Shiro, T. Asahi, H. Koshima, Walking and rolling of crystals induced thermally by phase transition. *Nat. Commun.* **9**, 538 (2018).
73. A. Mourran, H. Zhang, R. Vinokur, M. Möller, Soft microrobots employing nonequilibrium actuation via plasmonic heating. *Adv. Mater.* **29**, 1604825 (2017).

Acknowledgments

Funding: X.H. acknowledges funding from the American Chemical Society for award 66747-ND7, Johnson & Johnson for award 20231448, Inventor Fellow award 12072, NIH for award R01DK132319, the Moore Foundation Award 12072, Semiconductor Research

Corporation for award 2023-JU3136, and the Office of Naval Research (ONR) for awards N000142412187 and N000142212595. **Author contributions:** Conceptualization: C.C. and X.H. Methodology: C.C., Z.W., and Z.L. Investigation: C.C., Y.W., P.S., M.S., and W.H. Visualization: C.C. and S.D. Supervision: C.C. and X.H. Writing—original draft: C.C., Z.W., Y.W., P.S., Z.L., M.S., and X.H. Writing—review and editing: C.C., Z.W., Y.W., P.S., Z.L., and X.H. **Competing interests:** The authors declare that they have no competing interests. **Data, code, and materials availability:** All data and code needed to evaluate and reproduce the results in the paper are present in the paper and/or the Supplementary Materials. This study did not generate new materials. Contact X.H. (ximinhe@ucla.edu) for any questions.

Submitted 29 August 2025
Accepted 25 March 2026
Published 29 April 2026
10.1126/sciadv.aeb8948

ScienceAdvances

Twirlbot: Tumbleweed-inspired rolling robot

Chi Chen, Zhuo Wang, Yuchen Wang, Pengju Shi, Zixiao Liu, Muqing Si, Sidi Duan, Wenhao Hou, and Ximin He

Sci. Adv. **12** (18), eaeb8948. DOI: 10.1126/sciadv.aeb8948

Science Advances (ISSN 2375-2548) is published by the American Association for the Advancement of Science. 1200 New York Avenue NW, Washington, DC 20005. The title *Science Advances* is a registered trademark of AAAS.